

Growth and characterization of a $\text{Li}_2\text{Mg}_2(\text{MoO}_4)_3$ scintillating bolometer

F.A. Danevich^{a,b,*}, V.Ya. Degoda^c, L.L. Dulger^c, L. Dumoulin^b,
 A. Giuliani^{b,d}, P. de Marcillac^b, S. Marnieros^b, C. Nones^e, V. Novati^b,
 E. Olivieri^b, A.A. Pavlyuk^f, D.V. Poda^{a,b}, V.A. Trifonov^f, I.V. Yushina^f,
 A.S. Zolotarova^e

^a*Institute for Nuclear Research, 03028 Kyiv, Ukraine*

^b*CSNSM, Univ. Paris-Sud, CNRS/IN2P3, Université Paris-Saclay, 91405 Orsay, France*

^c*Kyiv National Taras Shevchenko University, 03127 Kyiv, Ukraine*

^d*DISAT, Università dell'Insubria, 22100 Como, Italy*

^e*IRFU, CEA, Université Paris-Saclay, F-91191 Gif-sur-Yvette, France*

^f*Nikolaev Institute of Inorganic Chemistry, 630090 Novosibirsk, Russia*

Abstract

Lithium magnesium molybdate ($\text{Li}_2\text{Mg}_2(\text{MoO}_4)_3$) crystals were grown by the low-thermal-gradient Czochralski method. Luminescence properties of the material (emission spectra, thermally stimulated luminescence, dependence of intensity on temperature, phosphorescence) have been studied under X-Ray excitation in the temperature interval from 8 K to 400 K, while at the same being operated as a scintillating bolometer at 20 mK for the first time. We demonstrated that $\text{Li}_2\text{Mg}_2(\text{MoO}_4)_3$ crystals are a potentially promising detector material to search for neutrinoless double beta decay of ^{100}Mo .

Keywords: Double beta decay, ^{100}Mo , Cryogenic scintillating bolometer, $\text{Li}_2\text{Mg}_2(\text{MoO}_4)_3$ crystal, Crystal growth, Luminescence

1. Introduction

Neutrinoless double beta ($0\nu 2\beta$) decay is of essential interest to particle physics since this process violates lepton number and requires the neutrino to be a massive Majorana particle [1, 2, 3, 4]. Generally speaking, $0\nu 2\beta$ decay can be mediated by many other beyond the Standard Model effects [5, 6].

*Corresponding author. E-mail: fedor.danevich@csnsm.in2p3.fr

Significant efforts have been made to observe the $0\nu 2\beta$ decay, however; the decay have yet to be observed (see the reviews [7, 8, 9, 10, 11] and recent results [12, 13, 14, 15, 16]). The experiments have set limits on the half-life of this process in the range of $T_{1/2} \sim 10^{24} - 10^{26}$ yr for various nuclei, allowing us to restrict the effective Majorana neutrino mass at the level of $\langle m_\nu \rangle \sim 0.1 - 0.8$ eV. The broad range of the neutrino mass limits results from the uncertainty of the nuclear matrix elements calculations [17].

The experimental sensitivity should be further improved to explore the inverted hierarchy of the neutrino mass ($\langle m_\nu \rangle \approx 0.02 - 0.05$ eV) corresponding to $T_{1/2} \sim 10^{26} - 10^{27}$ yr even for the most promising nuclei candidates [4, 17]. Experiments able to detect so rare $0\nu 2\beta$ decays should operate hundreds of kg of an isotope of interest, and have high detection efficiency and energy resolution, and a very low (ideally zero) background. Low temperature scintillating bolometers have a great potential to realize large-scale high-sensitivity $0\nu 2\beta$ decay experiments with several nuclei. The isotope ^{100}Mo is one of the most promising candidates thanks to the high endpoint energy of decay $Q_{2\beta} = 3034.36(17)$ keV [18], a high isotopic abundance $\delta = 9.744(65)\%$ [19] (and possibility of enrichment in large amount by gas-centrifugation), and a high decay probability [20, 21, 22, 23].

There are several molybdate crystals have already been tested as scintillating bolometers: ZnMoO_4 [24, 25, 26], Li_2MoO_4 [26, 27], $\text{Li}_2\text{Zn}_2(\text{MoO}_4)_3$ [28], CaMoO_4 [29] with their main properties reported in Table 1.

Table 1: Properties of Li_2MoO_4 , $\text{Li}_2\text{Mg}_2(\text{MoO}_4)_3$, $\text{Li}_2\text{Zn}_2(\text{MoO}_4)_3$, CaMoO_4 , and ZnMoO_4 crystal scintillators. Wavelength of scintillation emission maximum is denoted as λ_{max} , N_{vol} denotes number of Mo atoms per volume of the crystals.

Properties	Li_2MoO_4 [27]	$\text{Li}_2\text{Mg}_2(\text{MoO}_4)_3$	$\text{Li}_2\text{Zn}_2(\text{MoO}_4)_3$ [28]	CaMoO_4 [30]	ZnMoO_4 [31]
Density (g/cm^3)	3.02 – 3.07	3.89 [32] 3.798 [33] 3.82 (present work)	4.38	4.2 – 4.3	4.3
Melting point ($^\circ\text{C}$)	701	1033 [32]	890	1445 – 1480	1003
Structural type	Phenacite	Pnma [33, 34, 35]	Orthorhombic	Scheelite	Triclinic, $P1$
Hardness (Mohs)				3.5 – 4	3.5
λ_{max} (nm)	590	585 (present work)	610	520	625
Refractive index	1.44		2.0	1.98	1.89 – 1.96
Hygroscopicity	Weak	No	No	No	No
N_{vol} (atoms/ cm^3)	1.06×10^{22}	1.27×10^{22}	1.27×10^{22}	1.28×10^{22}	1.15×10^{22}

In addition to the technical requirements described above, a crystal scintillator for a large-scale high-sensitivity $0\nu 2\beta$ decay experiment should meet some practical requirements: low material cost, the capability for mass production, possibility of enriched molybdenum recycling to minimize loss of the enriched isotope, and to produce more scintillation elements. In a case of large scale cryogenic experiments (e.g., in the CUPID project [36, 37]), one should place a maximum number of the nuclei of interest in a restricted cryostat volume. From this point of view, the $\text{Li}_2\text{Mg}_2(\text{MoO}_4)_3$ crystal looks to be one of the most appropriate materials for cryogenic experiments with ^{100}Mo . Absence of hygroscopicity (in contrast to weak hygroscopicity of Li_2MoO_4) is also an advantage of the material.

In the present work, a $\text{Li}_2\text{Mg}_2(\text{MoO}_4)_3$ crystal has been investigated as possible low temperature scintillator for double beta decay experiments with ^{100}Mo . Crystal growth of the compound is reported in Sec. 2, the luminescent properties of the material are summarized in Sec. 3, and the first test of a $\text{Li}_2\text{Mg}_2(\text{MoO}_4)_3$ crystal sample as scintillating bolometer is described in Sec. 4.

2. Growth of $\text{Li}_2\text{Mg}_2(\text{MoO}_4)_3$ crystals

The main difficulty in the production of $\text{Li}_2\text{Mg}_2(\text{MoO}_4)_3$ crystals is the incongruent melting of the compound [32, 33]. This property makes it difficult to grow large volume crystals by the ordinary Czochralski technique from a stoichiometric compound. In the present study, $\text{Li}_2\text{Mg}_2(\text{MoO}_4)_3$ crystals were grown by using the low-thermal-gradient Czochralski method [38, 39]. The $\text{Li}_2\text{Mg}_2(\text{MoO}_4)_3$ compound for the crystal growth has been synthesized by mixing Li_2CO_3 , MgO and MoO_3 powders in the ratio $\text{Li}_2\text{Mg}_2(\text{MoO}_4)_3 : \text{Li}_2\text{MoO}_4 = 2 : 3$. In the first stage of the crystal R&D, a molybdenum oxide of 99.9% purity grade has been used, replaced by a 99.999% high purity MoO_3 in later development. The powders mixture was placed in a platinum crucible $\varnothing 70 \times 120$ mm covered by a tight platinum lid with a thin pipe, heated to a temperature 5 – 10 degrees higher than the melting temperature. The melt homogeneity was achieved mixing the melt by a platinum roller unit over 2 – 3 hours. The HX620 crystal growing set-up utilized a three-zone resistance furnace with weight monitoring. Several crystal boules have been grown from a crystal seed of [010] orientation with a pulling rate 1 – 5 mm per day [40]. Two $\text{Li}_2\text{Mg}_2(\text{MoO}_4)_3$ crystal boules produced from 99.9% and 99.999% purity MoO_3 are shown in Fig. 1.

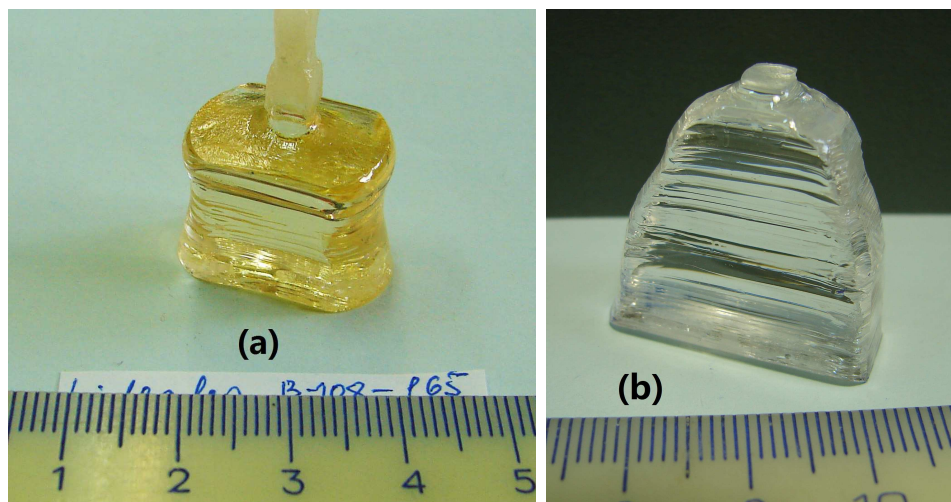


Figure 1: Boules of $\text{Li}_2\text{Mg}_2(\text{MoO}_4)_3$ crystals grown by the low-thermal-gradient Czochralski method from 99.9% (a) and 99.999% (b) purity grade MoO_3 . The improvement of the crystal's optical quality thanks to the utilization of the higher purity MoO_3 is clearly visible. The scales are in centimeters.

The higher optical quality of the $\text{Li}_2\text{Mg}_2(\text{MoO}_4)_3$ crystals produced from higher purity MoO_3 was confirmed by transmittance measurements performed with a Shimadzu UV-3101PC spectrometer. The results are presented in Fig. 2. The main cause of the crystals coloration is the contamination of the raw materials (particularly of the molybdenum oxide) by transition metals. The most abundant impurities of the 99.9% purity molybdenum oxide are K on the level of 0.01 wt%, and Si, Fe, Ti, Ni, Ca, Cr (0.001 wt%). Presence of Fe, Ti, Ni, Cr can lead to coloration of the crystal produced from the molybdenum oxide of the 99.9% purity grade. The effect of crystals coloration by transition metals is well known, and was also observed in molybdate crystals (see e.g. investigation of the raw-materials purity level on the optical quality of zinc molybdate crystal scintillators in [41]).

$\text{Li}_2\text{Mg}_2(\text{MoO}_4)_3$ crystals are isotypic with lithium zinc molybdate ($\text{Li}_2\text{Zn}_2(\text{MoO}_4)_3$) [35]. Therefore, one can assume that Li^+ and Mg^{2+} ions are distributed over the $M1$, $M2$ and $M3$ sites (see Fig. 4 in [35]). Taking into account that the composition of $\text{Li}_2\text{Mg}_2(\text{MoO}_4)_3$ crystals may depend on the synthesis temperature (as observed for $\text{Li}_2\text{Zn}_2(\text{MoO}_4)_3$ [33]), one can expect that the $\text{Li}_2\text{Mg}_2(\text{MoO}_4)_3$ crystal stoichiometry varies due to the sub-

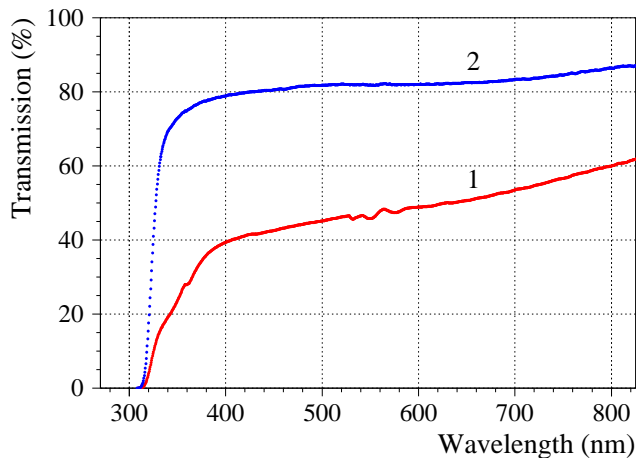


Figure 2: (Color online) Optical transmission curves of 2 mm of $\text{Li}_2\text{Mg}_2(\text{MoO}_4)_3$ crystals produced from 99.9% (1) and 99.999% (2) purity grade MoO_3 .

stitution/subtraction process $2\text{Li}^+ \rightarrow \text{Mg}^{2+} + \text{vacancy}$. Therefore, the real crystal composition is more accurately described by $\text{Li}_{2-2x}\text{Mg}_{2+x}(\text{MoO}_4)_3$, where $0 \leq x \leq 0.3$. However; the use of $\text{Li}_2\text{Mg}_2(\text{MoO}_4)_3$ compound in double beta decay or dark matter experiments would require a large number of identical crystals, with well-known compositions. It should be stressed that the composition of the produced $\text{Li}_2\text{Mg}_2(\text{MoO}_4)_3$ crystals is most strongly defined by the composition of the powder used for the crystal growth. And furthermore, it has been demonstrated in potassium gadolinium tungstate ($\text{KGd}(\text{WO}_4)_2$, a similar compound from the point of view of crystal growth), the low-thermal-gradient Czochralski method allowed to produce large volume (up to 200 cm^3), optically uniform $\text{KGd}(\text{WO}_4)_2$ crystals for laser applications [42]. R&D is already underway to produce high quality $\text{Li}_2\text{Mg}_2(\text{MoO}_4)_3$ crystal scintillators.

3. Luminescence of $\text{Li}_2\text{Mg}_2(\text{MoO}_4)_3$ crystal under X-Ray irradiation

The luminescence of a $\text{Li}_2\text{Mg}_2(\text{MoO}_4)_3$ crystal sample $10 \times 2 \times 2 \text{ mm}^3$ was investigated under X-Ray Irradiation (X-Ray Luminescence, XRL) in a wide temperature range from 8 K to 400 K. The sample was mounted on a copper holder inside a vacuum cryostat (a simplified scheme of the set-up is

presented in Fig. 3). The temperature of the copper holder was controlled by a semiconductor silicon sensor WAD305 (in the temperature interval 8 K – 85 K), and with a chromel-copel thermocouple (in the temperature interval 85 K – 450 K). We showed in separate measurements, that the temperature difference between a crystal sample and the support does not exceed 0.2 K (0.4 K upon linear heating of the sample). The crystal sample was irradiated through a beryllium window in the cryostat by X-Rays from an X-Ray tube BHV-7 with a rhenium anode operated at 20 kV, 25 mA with a flux of 0.635 mW/cm². The luminescence was measured in two spectral channels: in a wide wavelength interval (integral mode) and at a selected wavelength 548 nm (spectral mode). In the integral mode, the luminescence light was focused with the help of a quartz lens on the photocathode of a photomultiplier tube FEU-106 with extended sensitivity in the wavelength region of 350 – 820 nm. A high-transmission monochromator MDR-2 (with a 600 mm⁻¹ diffraction grating) was used in the spectral mode. The emission spectra were then corrected for the spectral sensitivity of the registration system. The temperature dependencies of the XRL intensity was obtained by cooling the sample to avoid effect of Thermally Stimulated Luminescence (TSL). Phosphorescence measurements were carried out after irradiation at temperatures of 8 K and 85 K over ≈ 10 minutes (the exposure dose was ≈ 0.8 J/cm²). The TSL of the sample was measured after the phosphorescence measurements while heating of the samples with a rate 0.30 ± 0.02 K/s.

The emission spectra of Li₂Mg₂(MoO₄)₃ crystal measured under X-Ray irradiation at 8 K, 85 K and 295 K are shown in Fig. 4. The main broad emission band with a maximum at ≈ 600 nm is observed at room and liquid nitrogen temperatures, while the position of the maximum is slightly shifted to a shorter wavelength ≈ 585 nm at 8 K. An additional infrared band appeared at ~ 750 nm with cooling of the sample to the liquid helium temperature. The measured emission spectra are slightly different from those observed under ultraviolet excitation with the maximum at 520 nm [43]. It should be stressed that the luminescence emission wavelength range of Li₂Mg₂(MoO₄)₃ crystal is suitable for application of the material as low temperature scintillating bolometer as discussed in Sec. 4. Indeed, the wide spectral sensitivity of germanium photodetectors (400 – 1700 nm [44]) covers the emission spectral range of the Li₂Mg₂(MoO₄)₃ crystal.

The dependencies of the Li₂Mg₂(MoO₄)₃ luminescence intensity on temperature measured in the integral and spectral modes are presented in Fig. 5. The luminescence intensity increases by more than three times by cooling the

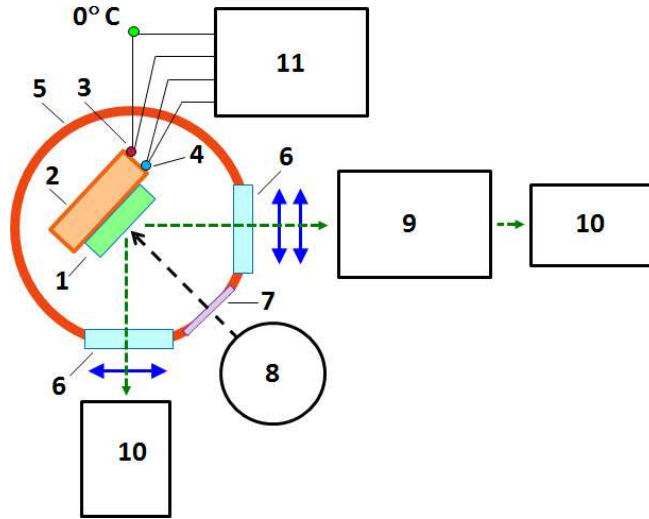


Figure 3: (Color online) Scheme of the set-up to study luminescence of the $\text{Li}_2\text{Mg}_2(\text{MoO}_4)_3$ crystal under X-Ray irradiation: (1) $\text{Li}_2\text{Mg}_2(\text{MoO}_4)_3$ crystal sample, (2) copper holder of the crystal sample, (3) thermocouple, (4) semiconductor silicon sensor, (5) vacuum cryostat, (6) quartz lens, (7) beryllium window, (8) X-Ray tube, (9) monochromator, (10) photomultiplier tube, (11) temperature measuring unit.

sample. Similar properties were observed in Li_2MoO_4 [27] and $\text{Li}_2\text{Zn}_2(\text{MoO}_4)_3$ [28]. Other molybdate crystals (as, e.g., CaMoO_4 [45], ZnMoO_4 [31], SrMoO_4 [46]) are also characterized by an increasing of luminescence and scintillation efficiency as they are cooled down to near liquid helium temperatures.

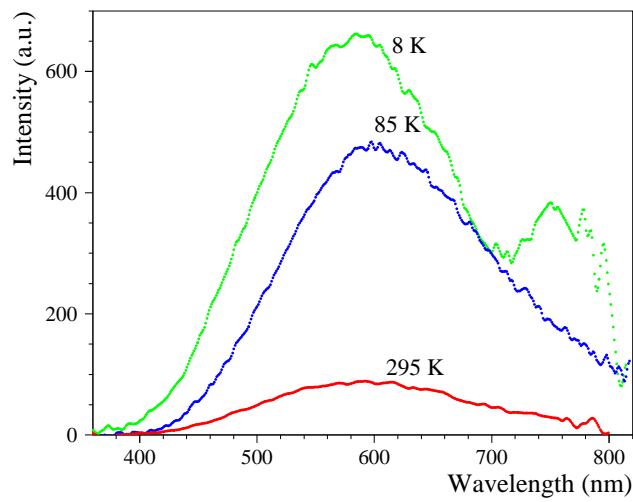


Figure 4: (Color online) Emission spectra of $\text{Li}_2\text{Mg}_2(\text{MoO}_4)_3$ crystal under X-Ray irradiation at 8 K, 85 K and 295 K.

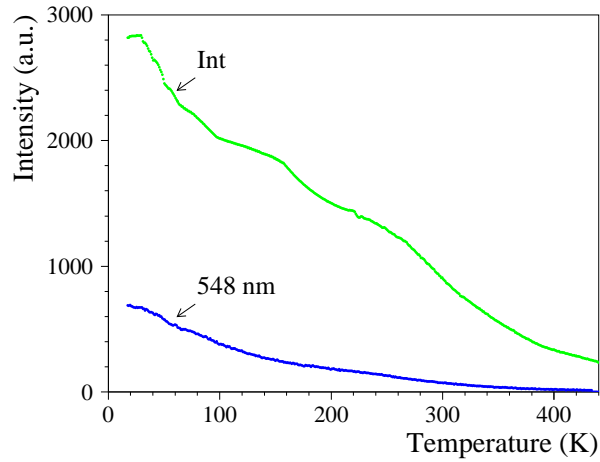


Figure 5: (Color online) Temperature dependencies of XRL intensity of $\text{Li}_2\text{Mg}_2(\text{MoO}_4)_3$ crystal measured in the integral ("Int") and spectral (at 548 nm) modes of measurements.

The luminescence intensity during X-Ray excitation in $\text{Li}_2\text{Mg}_2(\text{MoO}_4)_3$ crystal is almost constant at room temperature (see Fig. 6). A rather weak increase of the XRL intensity at 77 K by $\approx 12\%$ with a decrease at 8 K by $\approx 13\%$ after irradiation over 20 minutes were observed. A systematic error of the measurements does not exceeds $1.5\% - 3\%$. It should be noted that after heating the sample up to 450 K and then cooling again (without irradiation during the cooling) to low temperatures (8 K or 85 K), the dose dependencies of the XRL intensity remain the same. Taking into account the constant XRL intensity at 295 K, one could assume that the change in the XRL intensity at low temperatures is due to the processes of charge carriers accumulation in deep traps and recharging of recombination centers [47]. This hypothesis is also confirmed by the presence of phosphorescence and TSL described below. In general, the observed independence of the $\text{Li}_2\text{Mg}_2(\text{MoO}_4)_3$ luminescence on the dose (that is proportional to the duration of X-Ray irradiation) indicates a high radiation resistance of the material.

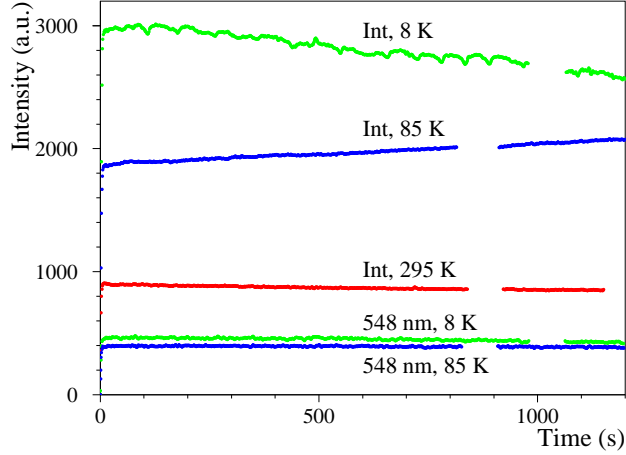


Figure 6: (Color online) Dependencies of $\text{Li}_2\text{Mg}_2(\text{MoO}_4)_3$ crystal XRL intensities on duration of X-Ray irradiation at 8 K, 85 K and 295 K. The data at 8 K and 85 K were recorded also in the spectral mode at 548 nm.

The $\text{Li}_2\text{Mg}_2(\text{MoO}_4)_3$ crystal showed a substantial phosphorescence, as one can see in Fig. 7, where the phosphorescence decay curves recorded at 8 K and 85 K are shown. As it was demonstrated for ZnMoO_4 crystals, long term phosphorescence can be described by three exponential functions better than by the Becquerel hyperbolic formula [47]. The fits of the $\text{Li}_2\text{Mg}_2(\text{MoO}_4)_3$ phosphorescence decay curves are presented in Fig. 7. E.g., for the phosphorescence at 85 K the decay times are $\tau_1 = 10(2)$ s, $\tau_2 = 42(5)$ s and $\tau_3 = 380(10)$ s, while at 8 K the decay times are $\tau_1 = 20(2)$ s, $\tau_2 = 91(12)$ s and $\tau_3 = 940(70)$ s. The τ_1 represents the effects of free charge recombination coupled with charge carriers delocalized from shallow traps, τ_2 and τ_3 stem from delocalization from phosphorescent traps and deep traps, respectively. The phosphorescence shows the recombination character of luminescence in $\text{Li}_2\text{Mg}_2(\text{MoO}_4)_3$. Similar phosphorescence properties were observed for ZnMoO_4 [47] and Li_2MoO_4 [27] crystals. The long term phosphorescence indicates that the material tends to have some afterglow, a well known effect in scintillators. However; the intensity of the signal due to afterglow after ~ 0.1 s of energy release in the $\text{Li}_2\text{Mg}_2(\text{MoO}_4)_3$ crystal (the time to analyze scintillation pulse profiles in low temperature scintillating bolometers is typically shorter) decreases by two orders of amplitude, approaching the photodetectors noise. Moreover; further improvement of the crystals quality should reduce the phosphorescence and possible afterglow effects.

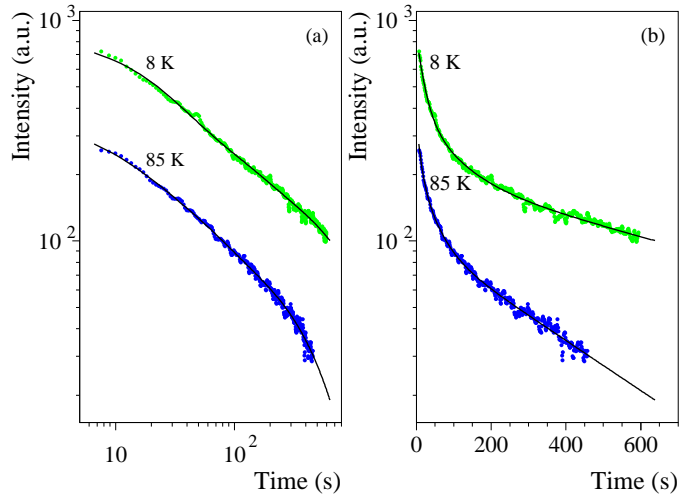


Figure 7: (Color online) The phosphorescence kinetic curves in double logarithmic (a) and logarithmic (b) scales measured with the $\text{Li}_2\text{Mg}_2(\text{MoO}_4)_3$ crystal after X-Ray irradiation at temperatures 8 K and 85 K.

The TSL of $\text{Li}_2\text{Mg}_2(\text{MoO}_4)_3$ crystal measured after X-Ray irradiation at 8 K and 85 K are presented in Fig. 8. It should be noted that use of two excitation temperatures allows more accurate investigations of TSL, since accumulation of charge carriers on the traps depends on the temperature of the excitation. The most intensive TSL peak is observed at ~ 225 K (similar to $\text{Li}_2\text{Zn}_2(\text{MoO}_4)_3$ [28]). At room temperature, the traps responsible for the TSL become shallow resulting in a stronger radiation resistance of the material (see Fig. 6).

Both the intensive phosphorescence and the TSL prove the presence of traps in the $\text{Li}_2\text{Mg}_2(\text{MoO}_4)_3$ crystal sample due to defects, which indicates that there is still room to improve the material.

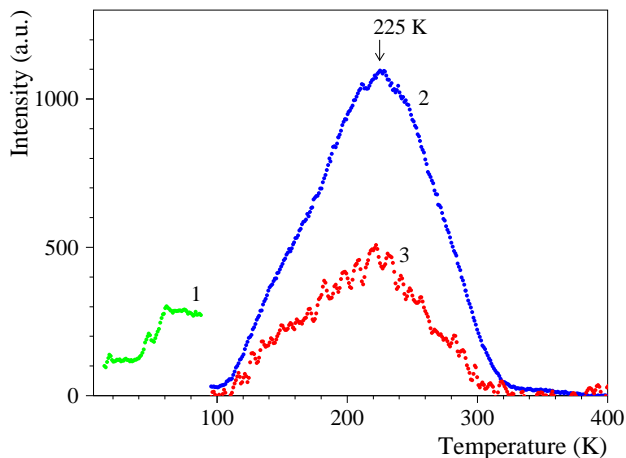


Figure 8: (Color online) Thermally stimulated luminescence of $\text{Li}_2\text{Mg}_2(\text{MoO}_4)_3$ crystal measured after X-Ray irradiation at temperature 8 K in integral mode (1), and at 85 K in integral (2) and spectral (3) modes.

4. Performance tests at milli-Kelvin temperature

A $\text{Li}_2\text{Mg}_2(\text{MoO}_4)_3$ crystal sample (10.24 g, $1.9 \times 1.4 \times 1.0 \text{ cm}^3$) was equipped with a Neutron Transmutation Doped (NTD) Ge thermistor and a silicon heater (for stabilization), which was than mounted in a copper frame (see Fig. 9 (a)) to run as bolometer.

Scintillation signals from the $\text{Li}_2\text{Mg}_2(\text{MoO}_4)_3$ crystal were recorded with the help of a photodetector operated at 60 V in Neganov-Luke mode [48, 49]. The photodetector (see Fig. 9 (b)) consists of a germanium disk 44 mm in diameter with a set of concentric annular Al electrodes with a pitch 3.7 mm and coated with a SiO anti-reflective film 70 nm thick (cyan color area on the picture). 60 V voltage was applied between the electrodes to amplify the scintillation signals. Heat signals after absorption of scintillation photons are read-out by an NTD germanium thermistor (visible in the lower part of the picture, attached at the germanium disk near the edge).

The detector module was run in a pulse-tube dilution refrigerator [50]. The set-up is located aboveground at the CSNSM (Orsay, France). A weak ^{210}Po alpha source was installed in the detector module to irradiate the crystal. The cryostat is surrounded by a massive low-activity lead shield with 10 cm maximum thickness to reduce environmental gamma background and

the soft component of cosmic rays. The data were acquired in stream mode with a 5 kHz sampling rate.

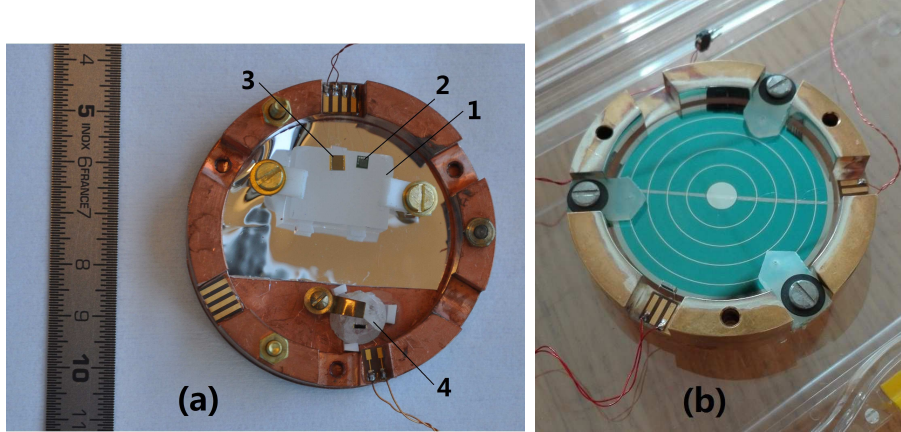


Figure 9: (Color online) (a) $\text{Li}_2\text{Mg}_2(\text{MoO}_4)_3$ crystal sample (1) fixed on the copper frame and equipped with an NTD Ge thermistor (2) and a silicon heater (3). (4) Another crystal tested in the same set-up. (b) A Neganov-Luke Ge light detector used to read out scintillation signals from the $\text{Li}_2\text{Mg}_2(\text{MoO}_4)_3$ crystal.

A background energy spectrum was gathered over 88 h with the $\text{Li}_2\text{Mg}_2(\text{MoO}_4)_3$ scintillating bolometer at 20 mK as shown in in Fig. 10. Several gamma peaks (gamma quanta of ^{214}Pb and ^{214}Bi , daughters of environmental ^{226}Ra) are visible in the spectrum which allowed us to calibrate the detector and estimate its energy resolution (full width at half maximum, FWHM) as shown in the Fig. 10. For instance, the energy resolution of the detector was measured as $\text{FWHM} = 5.5 \text{ keV}$ at 609 keV (gamma quanta of ^{214}Bi), while the baseline energy resolution of the detector module was 3.8 keV. The spectroscopic characteristics of a $\text{Li}_2\text{Mg}_2(\text{MoO}_4)_3$ -based detector could be further improved operating the device in lower-level background conditions and at lower temperature.

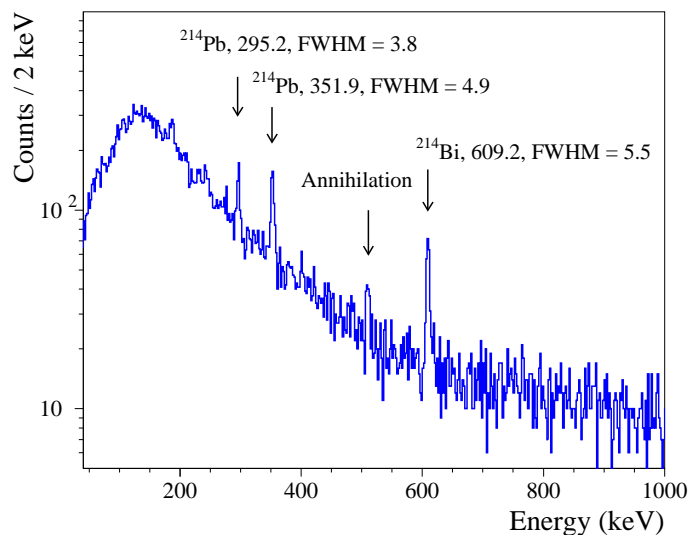


Figure 10: (Color online) Background energy spectrum accumulated over 88 h with a 10 g $\text{Li}_2\text{Mg}_2(\text{MoO}_4)_3$ scintillating bolometer at 20 mK. Energies of γ quanta and values of the energy resolution (FWHM) are in keV.

The particle discrimination capability of the detector (an important characteristic for application in rare-event searches) is demonstrated by Fig. 11 with data accumulated over 88 h with the $\text{Li}_2\text{Mg}_2(\text{MoO}_4)_3$ scintillating bolometer. The γ , β , and cosmic muon events are clearly separated from the α -triton and α events¹.

¹The events between the bands can be explained by pulses pile-ups due to comparatively slow response of bolometric detectors (the time window of $\text{Li}_2\text{Mg}_2(\text{MoO}_4)_3$ heat pulses is ~ 0.07 s). The pile-up events nature was checked by their pulse profile analysis.

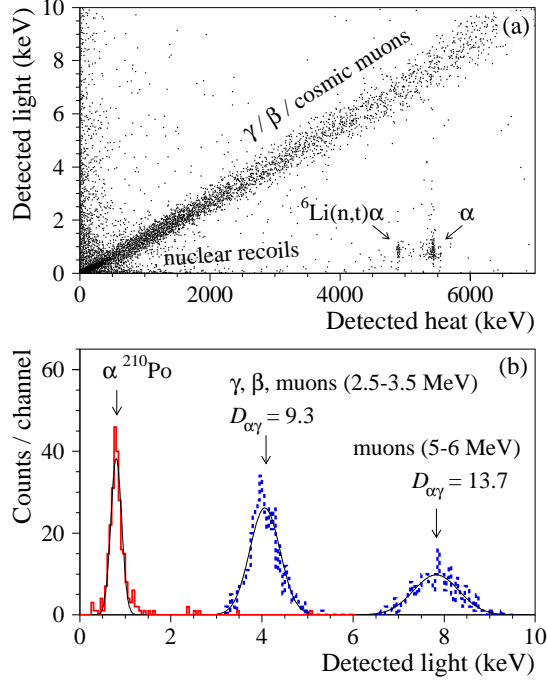


Figure 11: (Color online) (a) Scatter plot of the light versus the heat signal amplitudes accumulated with $\text{Li}_2\text{Mg}_2(\text{MoO}_4)_3$ scintillating bolometer over 88 h. The γ , β , muon events are clearly separated from the neutron induced nuclear recoils, α -triton, and α events of ^{210}Po . (b) Discrimination between α events of ^{210}Po (solid histogram) and γ , β , cosmic muons events in the energy intervals 2.5 – 3.5 MeV and 5 – 6 MeV (dashed histograms) with the discrimination power $D_{\alpha\gamma} = 9.3$ and $D_{\alpha\gamma} = 13.7$, respectively (see equation (1) for $D_{\alpha\gamma}$ definition). The fits of the distributions by Gaussian functions are shown by solid lines.

The particle discrimination capability (denoted here as $D_{\alpha\gamma}$) to discriminate α particles and γ quanta (β particles, muons) can be determined by the following formula:

$$D_{\alpha\gamma} = |A_\alpha - A_\gamma| / \sqrt{\sigma_\alpha^2 + \sigma_\gamma^2}, \quad (1)$$

where A (σ) are average values (standard deviations) of the scintillation signals distributions for α particles and γ quanta (or other particles such as betas and muons). We obtained $D_{\alpha\gamma} = 9.3(13.7)$ for 5.3 MeV α particles of ^{210}Po and γ (β , muons) events in the energy intervals 2.5 – 3.5 MeV (5 – 6 MeV). The distributions are shown in Fig. 11 (b). However, the

discrimination power should be estimated in the same energy interval for α particles and γ quanta (β particles) in the energy region of the $0\nu 2\beta$ peak of ^{100}Mo . Unfortunately, the statistic of α events with energy 2.5 – 3.5 MeV in our data is rather poor. We are going to utilize an α source emitting energy-degraded α particles to investigate the discrimination power of $\text{Li}_2\text{Mg}_2(\text{MoO}_4)_3$ -based scintillating bolometers in our further studies of the detector material. Nevertheless, the achieved discrimination power is high enough to discriminate β and α events in a double beta experiment with ^{100}Mo .

Moreover; some differences were observed in the heat-pulse shapes of γ (β , cosmic muons) and α events. For this analysis, we applied a parameter (pulse-shape parameter) that is a ratio between the fitted amplitude (a value of signal maximum obtained by the pulse fit) to the filtered amplitude (a signal maximum after applying the optimum filter [51, 52]). A background scatter plot of the pulse-shape parameter versus the heat signal amplitudes accumulated with the $\text{Li}_2\text{Mg}_2(\text{MoO}_4)_3$ scintillating bolometer over 88 h is presented in Fig. 12 (a). The distributions of the pulse-shape parameter for γ , β , muon events with energy 2.5–3.5 MeV, and α events of ^{210}Po are shown in Fig. 12 (b). The discrimination power for the distributions calculated by equation (1) is $D_{\alpha\gamma} = 1.6$.

The scintillation light yield of the $\text{Li}_2\text{Mg}_2(\text{MoO}_4)_3$ crystal scintillator (the detected light energy per particle energy measured by the deposited heat) is estimated to be 1.3 keV/MeV. The estimation was done thanks to the calibration of the photodetector by using 5.9 keV X-rays from a weak ^{55}Fe source. The value is comparable to the light yield observed with ZnMoO_4 (0.8 – 1.5 keV/MeV) and slightly exceeds the light yield of Li_2MoO_4 crystal scintillators (0.7 – 1.0 keV/MeV) [26].

The quenching factor for α particles in the $\text{Li}_2\text{Mg}_2(\text{MoO}_4)_3$ scintillator was estimated as the ratio between the detected scintillation signals amplitudes for α particles of ^{210}Po (in the energy interval around the α peak 5216 – 5411 keV) and the scintillation signals amplitudes for cosmic muons (γ quanta, β particles) in the same energy interval as 0.105(2).

An energy spectrum of the α -triton and α events accumulated by the $\text{Li}_2\text{Mg}_2(\text{MoO}_4)_3$ scintillating bolometer was built by using the difference in scintillation yield presented in Fig. 11. The obtained energy spectrum is shown in Fig. 13. There are two clearly visible groups of events in the data: α -triton peak with energy 4784 keV caused by thermal neutrons capture on ^6Li , and two peaks of ^{210}Po . One peak is from the ^{210}Po alpha source

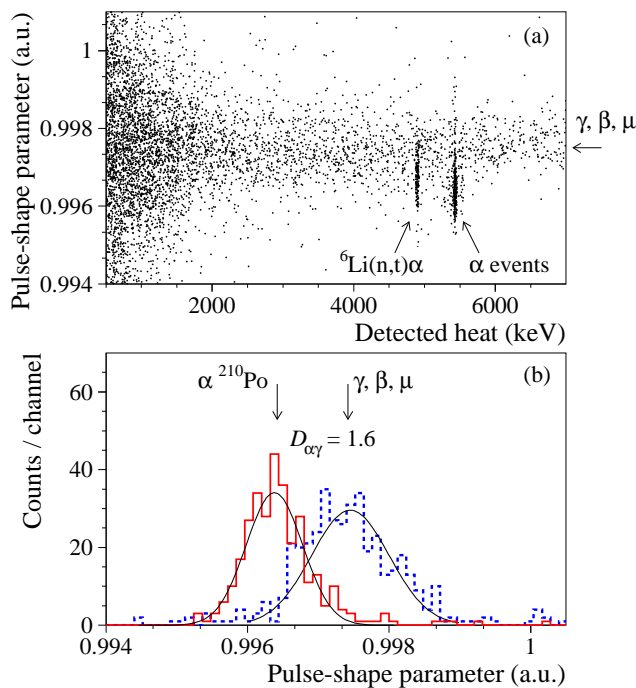


Figure 12: (Color online) (a) Scatter plot of the pulse-shape parameter (see text) versus the heat signal amplitudes accumulated with $\text{Li}_2\text{Mg}_2(\text{MoO}_4)_3$ scintillating bolometer over 88 h of background run. (b) The positions of the pulse-shape parameter distributions for α events of ${}^{210}\text{Po}$ (solid histogram), and for the γ, β, μ events with energy 2.5 – 3.5 MeV (dashed histogram) are slightly different due to the difference in the heat signals shape. Fits of the distributions by Gaussian functions are shown by solid lines.

that irradiated the crystal (the peak is labelled in Fig. 13 as “ ${}^{210}\text{Po}$ ext”), while the second weak peak is due to the bulk contamination of the crystal by ${}^{210}\text{Po}$ (labelled on the Figure as “ ${}^{210}\text{Po}$ int”). The energy resolution is $\text{FWHM} \approx 12$ keV for the α -triton peak, and $\text{FWHM} \approx 9$ keV for the internal ${}^{210}\text{Po}$ peak.

Analysis of the alpha spectrum allowed us to evaluate radioactive contamination of the $\text{Li}_2\text{Mg}_2(\text{MoO}_4)_3$ crystal. Activity of the bulk ${}^{210}\text{Po}$ can be estimated as 5.6(1.3) mBq/kg, which is rather low taking into account that no particular efforts were made to obtain radiopure material. It should be stressed that we cannot conclude whether the ${}^{210}\text{Po}$ is result of the crystal contamination by ${}^{210}\text{Pb}$ or it is ${}^{210}\text{Po}$ itself. If it is polonium contamination then the activity should decrease substantially within a few years, due to

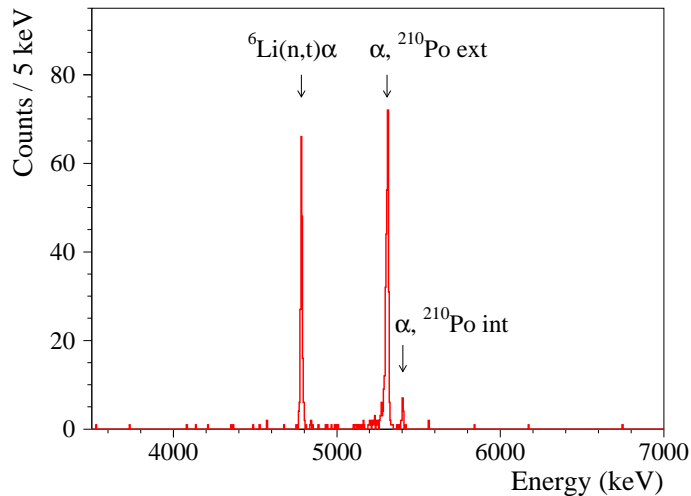


Figure 13: (Color online) Background energy spectrum of the α -triton and α events accumulated by the $\text{Li}_2\text{Mg}_2(\text{MoO}_4)_3$ scintillating bolometer over 88 h.

the comparatively short half-life of ^{210}Po : $T_{1/2} \approx 138$ d. In contrast, the activity of ^{210}Po could even increase (see, e.g., Fig. 7 in [53]) in the case of lead (^{210}Pb) contamination (the half-life of ^{210}Pb is $T_{1/2} \approx 22$ yr, the crystal was produced approximately 9 months before the test). Due to the absence of other α peaks we were only able to set limits (lim A) on the active alpha members of the ^{235}U , ^{238}U and ^{232}Th chains with the equation (2):

$$\text{lim } A = \text{lim } S / (\varepsilon \cdot \theta \cdot m \cdot t) \quad (2)$$

where ε is the detection efficiency (assumed to be 100% due to a very short path length of alpha particles in the $\text{Li}_2\text{Mg}_2(\text{MoO}_4)_3$ crystal), θ is the α particle emission probability, m is the mass of the crystal sample, t is the measuring time, and lim S is the number of α events that can be excluded at a given confidence level (C.L., all the limits here are given with 90% C.L.). Values of lim S were estimated by using the Feldman-Cousins procedure for no effect observed on an estimated background [54]. The measured numbers of events were calculated in the energy intervals ± 30 keV around the Q_α of the expected α peaks (the interval is wider than ± 3 sigma for all expected α peaks, therefore, the detection efficiency remains almost 100%), while the background counting rate was estimated in the energy intervals 3.3 – 4 MeV and 4.35 – 4.65 MeV, where no α particles of U/Th are expected. For in-

stance, in the energy interval 4052 – 4112 keV (where a peak of ^{232}Th with energy 4081.6 keV is expected) 1 event was detected, while the estimated background is 1.32 counts. Therefore, according to [54] we should exclude $\lim S = 3.06$ counts, that lead to the limit on ^{232}Th activity in the crystal ≤ 0.95 mBq/kg. Other limits were obtained in a similar way. A summary of the $\text{Li}_2\text{Mg}_2(\text{MoO}_4)_3$ crystal radioactive contamination is presented in Table 2.

Table 2: Radioactive contamination of the $\text{Li}_2\text{Mg}_2(\text{MoO}_4)_3$ crystal.

Chain	Sub-chain	Activity (mBq/kg)
^{232}Th	^{232}Th	≤ 0.95
	^{228}Th	≤ 1.1
^{238}U	^{238}U	≤ 0.95
	^{234}U	≤ 1.7
	^{226}Ra	≤ 1.7
	^{210}Po	5.6(1.3)
^{235}U	^{235}U	≤ 1.9
	^{223}Ra	≤ 1.1

5. Conclusions

Large volume optically-clear quality $\text{Li}_2\text{Mg}_2(\text{MoO}_4)_3$ crystals were grown with the help of the low-thermal-gradient Czochralski method. The luminescence of a $\text{Li}_2\text{Mg}_2(\text{MoO}_4)_3$ crystal sample was studied under X-Ray excitation in the 8 – 400 K temperature range. Luminescence with a maximum at 585 nm is observed at 8 K. The luminescence intensity increases by more than a factor 3 when cooling the crystal sample from room temperature to 8 K. Intense phosphorescence and thermally stimulated luminescence indicate presence of traps due to defects in the crystal sample, which points to that fact that the material quality can be further improved.

Low temperature measurements (at 20 mK) of a 10 g sample of $\text{Li}_2\text{Mg}_2(\text{MoO}_4)_3$ scintillating bolometer were carried out over 88 h, demonstrating energy resolution as good as 5.5 keV (FWHM, at 609 keV), despite the comparatively high baseline noise (3.8 keV, whereas it is typically on the level of 1 – 2 keV). The scintillator light yield is estimated as ≈ 1.3 keV/MeV. The

$\text{Li}_2\text{Mg}_2(\text{MoO}_4)_3$ scintillating bolometer showed an excellent particle discrimination capability with a discrimination power $D_{\alpha\gamma} = 9$ (see equation 1) for 2.5 – 3.5 MeV γ (β , muons) events and 5.3 MeV α particles of ^{210}Po . We have observed also a weak difference in the heat signal shapes of γ (β , cosmic muons) and α particles. Despite no special efforts to obtain radiopure material, the radioactive contamination of the crystal was measured to be quite low. The activity of ^{210}Po is ~ 6 mBq/kg, while only limits on the \sim mBq/kg level were estimated for other α active members of the ^{235}U , ^{238}U and ^{232}Th families. These bolometric measurements have demonstrated that $\text{Li}_2\text{Mg}_2(\text{MoO}_4)_3$ is a potentially promising detector material for double beta decay experiments with molybdenum as well as other rare-event searches.

In particular, we would like to stress that $\text{Li}_2\text{Mg}_2(\text{MoO}_4)_3$ scintillator contains a variety of elements with different atomic masses $A \approx 7, 16, 24, 96$ (Li, O, Mg and Mo, respectively) which can be exploited in dark matter low temperature scintillating bolometers (see CRESST [55]) to probe new areas of parameter space, particularly of spin-dependent dark matter.

6. Acknowledgements

These studies were supported in part by the project “Investigation of neutrino and weak interaction in double beta decay of ^{100}Mo ” in the framework of the Programme “Dnipro” based on Ukraine-France Agreement on Cultural, Scientific and Technological Cooperation, and by the IDEATE International Associated Laboratory (LIA). F.A. Danevich gratefully acknowledges the support from the “Jean d’Alembert” Grants program (Project CYGNUS) of the University of Paris-Saclay. A.S. Zolotarova is supported by the “IDI 2015” project funded by the IDEX Paris- Saclay, ANR-11-IDEX-0003-02. The authors are grateful to Alexander Leder from the Massachusetts Institute of Technology for a careful reading of the manuscript and helpful corrections.

References

- [1] J. Barea, J. Kotila, F. Iachello, Limits on Neutrino Masses from Neutrinoless Double- β Decay, *Phys. Rev. Lett.* 109 (2012) 042501.
- [2] W. Rodejohann, Neutrino-less double beta decay and particle physics, *J. Phys. G* 39 (2012) 124008.

- [3] S. Dell’Oro, S. Marcocci, M. Viel, F. Vissani, Neutrinoless Double Beta Decay: 2015 Review, AHEP 2016 (2016) 2162659.
- [4] J.D. Vergados, H. Ejiri, F. Šimkovic, Neutrinoless double beta decay and neutrino mass, Int. J. Mod. Phys. E 25 (2016) 1630007.
- [5] F.F. Deppisch, M. Hirsch, H. Päs, Neutrinoless double-beta decay and physics beyond the standard model, J. Phys. G 39 (2012) 124007.
- [6] S.M. Bilenky, C. Giunti, Neutrinoless double-beta decay: A probe of physics beyond the Standard Model, Int. J. Mod. Phys. A 30 (2015) 1530001.
- [7] S.R. Elliott, Recent progress in double beta decay, Mod. Phys. Lett. A 27 (2012) 123009.
- [8] A. Giuliani, A. Poves, Neutrinoless Double-Beta Decay, AHEP 2012 (2012) 857016.
- [9] O. Cremonesi, M. Pavan, Challenges in Double Beta Decay, AHEP 2014 (2014) 951432.
- [10] J.J. Gómez-Cadenas, J. Martín-Albo, Phenomenology of Neutrinoless Double Beta Decay, Proc. of Sci. (GSSI14) 004 (2015) 1.
- [11] X. Sarazin, Review of Double Beta Experiments, J. Phys.: Conf. Ser. 593 (2015) 012006.
- [12] J.B. Albert et al. (The EXO-200 Collaboration), Search for Majorana neutrinos with the first two years of EXO-200 data, Nature 510 (2014) 229.
- [13] R. Arnold et al., Results of the search for neutrinoless double- β decay in ^{100}Mo with the NEMO-3 experiment, Phys. Rev. D 92 (2015) 072011.
- [14] K. Alfonso et al. (CUORE Collaboration), Search for Neutrinoless Double-Beta Decay of ^{130}Te with CUORE-0, Phys. Rev. Lett. 115 (2015) 102502.
- [15] M. Agostini et al., Background-free search for neutrinoless double- β decay of ^{76}Ge with GERDA, Nature 544 (2017) 47.

- [16] A. Gando et al. (KamLAND-Zen Collaboration), Search for Majorana Neutrinos Near the Inverted Mass Hierarchy Region with KamLAND-Zen, *Phys. Rev. Lett.* 117 (2016) 082503.
- [17] J. Engel, J. Menéndez, Status and future of nuclear matrix elements for neutrinoless double-beta decay: a review, *Rep. Prog. Phys.* 80 (2017) 046301.
- [18] M. Wang et al., The AME2016 atomic mass evaluation, *Chin. Phys. C* 41 (2017) 030003.
- [19] J. Meija et al., Isotopic compositions of the elements 2013 (IUPAC Technical Report), *Pure Appl. Chem.* 88 (2016) 293.
- [20] T.R. Rodryguez, G. Martynez-Pinedo, Energy Density Functional Study of Nuclear Matrix Elements for Neutrinoless $\beta\beta$ Decay, *Phys. Rev. Lett.* 105 (2010) 252503.
- [21] F. Šimkovic, V. Rodin, A. Faessler, P. Vogel, $0\nu\beta\beta$ and $2\nu\beta\beta$ nuclear matrix elements, quasiparticle random-phase approximation, and isospin symmetry restoration, *Phys. Rev. C* 87 (2013) 045501.
- [22] J. Hyvarinen, J. Suhonen, Nuclear matrix elements for $0\nu 2\beta$ decays with light or heavy Majorana-neutrino exchange, *Phys. Rev. C* 91 (2015) 024613.
- [23] J. Barea, J. Kotila, F. Iachello, $0\nu 2\beta$ and $2\nu 2\beta$ nuclear matrix elements in the interacting boson model with isospin restoration, *Phys. Rev. C* 91 (2015) 034304.
- [24] J.W. Beeman et al., A next-generation neutrinoless double beta decay experiment based on ZnMoO_4 scintillating bolometers, *Phys. Lett. B* 710 (2012) 318.
- [25] J.W. Beeman et al., ZnMoO_4 : A promising bolometer for neutrinoless double beta decay searches, *Astropart. Phys.* 35 (2012) 813.
- [26] E. Armengaud et al., Development of ^{100}Mo -containing scintillating bolometers for a high-sensitivity neutrinoless double-beta decay search, *Eur. Phys. J. C* 77 (2017) 785.

- [27] T.B. Bekker et al., Aboveground test of an advanced Li_2MoO_4 scintillating bolometer to search for neutrinoless double beta decay of ^{100}Mo , *Astropart. Phys.* 72 (2016) 38.
- [28] N.V. Bashmakova et al., $\text{Li}_2\text{Zn}_2(\text{MoO}_4)_3$ as a potential detector for ^{100}Mo 2β search, *Functional Materials* 16 (2009) 266.
- [29] G.B. Kim et al., A CaMoO_4 Crystal Low Temperature Detector for the AMoRE Neutrinoless Double Beta Decay Search, *AHEP 2015* (2015) 817530.
- [30] A.N. Annenkov et al., Development of CaMoO_4 crystal scintillators for a double beta decay experiment with ^{100}Mo , *Nucl. Instrum. Meth. A* 584 (2008) 334.
- [31] D.M. Chernyak et al., Optical, luminescence and thermal properties of radiopure ZnMoO_4 crystals used in scintillating bolometers for double beta decay search, *Nucl. Instrum. Meth. A* 729 (2013) 856.
- [32] V.G. Penkova, P.V. Klevtsov, Synthesis of crystals of double lithium molybdates with Mg, Ni, Co, Fe and Zn divalent metals, *J. Inorg. Chem.* 22 (1977) 1713 (in Russian).
- [33] L. Sebastian et al., Synthesis, structure and lithium-ion conductivity of $\text{Li}_{2-2x}\text{Mg}_{2+x}(\text{MoO}_4)_3$ and $\text{Li}_3\text{M}(\text{MoO}_4)_3$ ($\text{M}^{\text{III}} = \text{Cr}, \text{Fe}$), *J. Mater. Chem.* 13 (2003) 1797.
- [34] R.F. Klevtsova, S.A. Magarill, Crystal Structure of lithium iron molybdates $\text{Li}_3\text{Fe}^{\bullet\bullet\bullet}(\text{MoO}_4)_3$ and $\text{Li}_3\text{Fe}_2^{\bullet\bullet}(\text{MoO}_4)_3$, *Crystallography Rep.* 15 (1970) 710 (in Russian).
- [35] S.F. Solodovnikov et al., Revised phase diagram of Li_2MoO_4 – ZnMoO_4 system, crystal structure and crystal growth of lithium zinc molybdate, *J. Solid State Chem.* 182 (2009) 1935.
- [36] G. Wang et al., CUPID: CUORE (Cryogenic Underground Observatory for Rare Events) Upgrade with Particle Identification, arXiv:1504.03599v1 [physics.ins-det].
- [37] G. Wang et al., R&D towards CUPID (CUORE Upgrade with Particle Identification), arXiv:1504.03612v1 [physics.ins-det].

- [38] A.A. Pavlyuk et al., Low Thermal Gradient technique and method for large oxide crystals growth from melt and flux, in the proceedings of the APSAM-92 (Asia Pacific Society for Advanced Materials), Shanghai, China, 26-29 April 1992, p. 164.
- [39] V.A. Trifonov et al., Growth and spectroscopic characteristics of $\text{Li}_2\text{Mg}_2(\text{MoO}_4)_3$ and $\text{Li}_2\text{Mg}_2(\text{MoO}_4)_3:\text{Co}^{2+}$ crystals, *Inorg. Mater.* 49 (2013) 517.
- [40] A.A. Pavlyuk, V.A. Trifonov, An approach to grow lithium magnesium molybdate, Patent No. 2487968, 2011, Russian Federation.
- [41] L. Bergé et al., Purification of molybdenum, growth and characterization of medium volume ZnMoO_4 crystals for the LUMINEU program, *JINST* 9 (2014) P06004.
- [42] M.M Mazur et al., Elastic and photoelastic properties of $\text{KGd}(\text{WO}_4)_2$ single crystals, *Akusticheskiy zhurnal* 58 (2012) 701 (in Russian).
- [43] A.A. Ryadun et al., Structure and properties of $\text{Li}_{2-2x}\text{Mg}_{2+x}(\text{MoO}_4)_3$ crystals activated by copper ions, *J. Struct. Chem.* 57 (2016) 459.
- [44] T.C. Larason and S.S. Bruce, Spatial uniformity of responsivity for silicon, gallium nitride, germanium, and indium gallium arsenide photodiodes, *Metrologia* 35 (1998) 491.
- [45] V.B. Mikhailik, S. Henry, H. Kraus, I. Solskii, Temperature dependence of CaMoO_4 scintillation properties, *Nucl. Instrum. Meth. A* 583 (2007) 350.
- [46] V.B. Mikhailik et al., Temperature dependence of scintillation properties of SrMoO_4 , *Nucl. Instrum. Meth. A* 792 (2015) 1.
- [47] V.Ya. Degoda et al., Long time phosphorescence in ZnMoO_4 crystals, *J. Luminescence* 181 (2017) 269.
- [48] B.S. Neganov, V.N. Trofimov, USSR Patent No. 1037771 (1981).
- [49] P.N. Luke, Voltage-assisted calorimetric ionization detector, *J. Appl. Phys.* 64 (1988) 6858.

- [50] M. Mancuso et al., An aboveground pulse-tube-based bolometric test facility for the validation of the LUMINEU ZnMoO_4 crystals, *J. Low Temp. Phys.* 176 (2014) 571.
- [51] V. Radeka, N. Karlovac, Least-square-error amplitude measurement of pulse signals in presence of noise, *Nucl. Instrum. Meth.* 52 (1967) 86.
- [52] E. Gatti, P.F. Manfredi, Processing the signals from solid-state detectors in elementary-particle physics, *Riv. Nuovo Cimento* 9 (1986) 1.
- [53] F.A. Danevich et al., Effect of recrystallisation on the radioactive contamination of CaWO_4 crystal scintillators, *Nucl. Instrum. Meth.* 631 (2011) 44.
- [54] G.J. Feldman, R.D. Cousins, Unified approach to the classical statistical analysis of small signals, *Phys. Rev. D* 57 (1998) 3873.
- [55] G. Angloher et al., Results on light dark matter particles with a low-threshold CRESST-II detector, *Eur. Phys. J. C* 76 (2016) 25.